

# Uniform Synthesis of Bilayer Hydrogen Substituted Graphdiyne for Flexible Piezoresistive Applications

Mukkath Joseph Josline, Soheil Ghods, Saikiran Kosame, Jun-Hui Choi, Woongchan Kim, Sein Kim, SooHyun Chang, Sang Hwa Hyun, Seung-II Kim, Ji-Yun Moon, Hyeong Gi Park, Sung Beom Cho, Heongkyu Ju, and Jae-Hyun Lee\*

Graphdiyne (GDY) has garnered significant attention as a cutting-edge 2D material owing to its distinctive electronic, optoelectronic, and mechanical properties, including high mobility, direct bandgap, and remarkable flexibility. One of the key challenges hindering the implementation of this material in flexible applications is its large area and uniform synthesis. The facile growth of centimeter-scale bilayer hydrogen substituted graphdiyne (Bi-HsGDY) on germanium (Ge) substrate is achieved using a low-temperature chemical vapor deposition (CVD) method. This material's field effect transistors (FET) showcase a high carrier mobility of  $52.6 \text{ cm}^2 \text{ V}^{-1} \text{ s}^{-1}$  and an exceptionally low contact resistance of  $10 \Omega \mu\text{m}$ . By transferring the as-grown Bi-HsGDY onto a flexible substrate, a long-distance piezoresistive strain sensor is demonstrated, which exhibits a remarkable gauge factor of 43.34 with a fast response time of  $\approx 275 \text{ ms}$ . As a proof of concept, communication by means of Morse code is implemented using a Bi-HsGDY strain sensor. It is believed that these results are anticipated to open new horizons in realizing Bi-HsGDY for innovative flexible device applications.

M. J. Josline, S. Ghods, J.-H. Choi, W. Kim, S. Kim, S. Chang, S. H. Hyun, S.-I. Kim, S. B. Cho, J.-H. Lee

Department of Materials Science and Engineering  
Ajou University

Suwon 16499, South Korea  
E-mail: [jaehyunlee@ajou.ac.kr](mailto:jaehyunlee@ajou.ac.kr)

M. J. Josline, S. Ghods, S. Kosame, J.-H. Choi, W. Kim, S. Kim, S. Chang, S. H. Hyun, S.-I. Kim, S. B. Cho, J.-H. Lee

Department of Energy Systems Research  
Ajou University

Suwon 16499, South Korea

S. Kosame, H. Ju  
Department of Physics  
Gachon University

Seongnam South Korea

S.-I. Kim, J.-Y. Moon  
Department of Mechanical Engineering and Materials Science

Washington University in Saint Louis

Saint Louis, MO, USA

H. G. Park  
AI-Superconvergence KIURI Translational Research Center

Ajou University  
School of Medicine

Suwon 16499, South Korea

 The ORCID identification number(s) for the author(s) of this article can be found under <https://doi.org/10.1002/smll.202307276>

DOI: 10.1002/smll.202307276

## 1. Introduction

Flexible strain sensors have sparked a revolution in a multitude of groundbreaking applications across diverse sectors, encompassing wearable electronics,<sup>[1]</sup> communication,<sup>[2]</sup> healthcare monitoring,<sup>[3]</sup> military,<sup>[4]</sup> and environmental sensing.<sup>[5]</sup> Large-area uniform 2D materials have emerged as highly promising choices for flexible strain sensing applications due to their outstanding properties including excellent mechanical flexibility,<sup>[6]</sup> stability,<sup>[7,8]</sup> and high surface-to-volume ratios.<sup>[9,10]</sup> Among the large assortment of 2D materials, carbon allotropes are considered exceptional candidates owing to their remarkable electrical conductivity,<sup>[11]</sup> high flexibility,<sup>[12]</sup> tunable properties,<sup>[13]</sup> ease of large-area processing,<sup>[14]</sup> and compatibility with polymer substrates.<sup>[15]</sup>

Hydrogen substituted graphdiyne (HsGDY), which belongs to the family of artificial carbon allotropes, is a notable candidate for strain sensors due to its unique characteristics such as finite bandgap,<sup>[16]</sup> inherent mechanical stability,<sup>[17]</sup> enhanced chemical stability,<sup>[18]</sup> and tailored properties.<sup>[19]</sup> Recently, a few-layer HsGDY has been reported to exhibit piezoresistive strain sensing abilities with fast response and applications in physiological monitoring.<sup>[20]</sup> Though the reports on HsGDY are limited, its unique properties and theoretical analyses of its characteristics punctuate the high potential of HsGDY for applications in strain sensors.<sup>[21]</sup>

The bottom-up growth of HsGDY mainly utilizes metal-catalyzed coupling reactions such as Sonogashira coupling<sup>[22]</sup> and Glaser coupling,<sup>[23,24]</sup> which creates many limitations in size, purity, uniformity, and thickness control of HsGDY, and thus limits the application of these materials in electronics.<sup>[25]</sup> Consequently, there is an urgent need for alternative growth approaches to overcome these challenges and facilitate the synthesis of high-quality HsGDY in large areas.

The CVD method is highly qualified to achieve an on-surface synthesis of high-quality, large-area ultrathin HsGDY on a substrate at low-temperature conditions. In recent years, metal substrates such as Ag and Cu have been used for the growth of HsGDY. Despite improvements in properties such as thickness control and purity of HsGDY, issues such as small size and

non-uniformity due to limitations of the substrate, hinder the utilization of this material in real electronic applications.<sup>[20,26]</sup> By utilizing Hexaethylbenzene (HEB) and 1,3,5-Triethylbenzene (TEB) as precursors, the  $\gamma$ -GDY and HsGDY films grown on Ag substrate show poor electronic properties (conductivity of 6.72 and  $0.27 \text{ S cm}^{-1}$ ) due to undesired side reactions that occur during the growth process.<sup>[26]</sup> On the other hand, HsGDY grown over Cu is affected by the high roughness of the Cu substrate, diminishing the quality of the layers and resulting in reduced carrier mobility. So, this limitation hinders sensor applications of this material.<sup>[20,27,28]</sup> Thus, it is important to choose an appropriate catalyst that would allow the growth of high-quality, uniform HsGDY in large areas that would have high sensitivity to even minute strains.

In this study, we have made significant strides in achieving the growth of highly uniform bilayer hydrogen substituted graphdiyne (Bi-HsGDY) on a flat Ge (110) substrate. The growth process involved utilizing TEB as a precursor in a low-temperature CVD process, specifically at 150 °C. Our Bi-HsGDY exhibited p-type characteristics, featuring an augmented carrier concentration of  $2.1 \times 10^{14} \text{ cm}^{-2}$  and notable carrier mobility of  $52.6 \text{ cm}^2 \text{ V}^{-1} \text{ s}^{-1}$ . Furthermore, by transferring the transparent large-area Bi-HsGDY onto flexible polyethylene terephthalate (PET) substrates, we gained valuable insights into electromechanical properties and long-distance piezoresistive Bi-HsGDY strain sensors. The observed enhanced strain sensitivity in Bi-HsGDY is attributed to the charge scattering effect at grain boundaries within its polycrystalline structure, surpassing the performance in the literature. We subsequently conducted a compelling demonstration to showcase the generation of Morse code. This demonstration serves as a testament to the potential applicability of our device in the field of ultra-sensitive strain sensors.

## 2. Results and Discussion

Lee et.al. have previously demonstrated remarkable milestones in growing high-quality, uniform, large-area monolayer graphene on a Ge substrate.<sup>[29]</sup> This notable success is primarily attributed to the excellent catalytic effect of Ge,<sup>[30]</sup> the uniformity of the substrate,<sup>[31]</sup> and the remarkably low carbon solubility of Ge.<sup>[32]</sup> Given the proven superiority of Ge as a growth substrate for graphene, we made a deliberate decision to choose it for the growth of HsGDY. A schematic for the CVD growth of HsGDY on a Ge substrate is shown in Figure 1a. There are different steps occurring during the growth process, including stage 1, adsorption of TEB molecules on the Ge surface; stage 2, Ge-catalyzed dehydrogenative coupling of TEB molecules which results in HsGDY clusters; and stage 3, formation of the HsGDY.<sup>[26,33]</sup> The surface-mediated growth mechanism is activated by the limited carbon solubility of Ge, enabling the constrained adsorption of TEB precursors onto the substrate and thereby supporting the formation of HsGDY with a bilayer structure (Figure S1, Supporting Information).

The HsGDY showcases an extended  $\pi$ -conjugated carbon framework, featuring benzene rings interconnected by butadiyne linkages and aromatic hydrogen atoms. This intricate structure ensures excellent electrical conductivity and contributes to its overall exceptional performance.<sup>[34]</sup> The temperature profile versus time during the whole synthesis protocol is shown in

Figure S2 (Supporting Information). Also, various parameters for the growth of HsGDY, including temperature, pressure, growth time, and carrier gas flow, were optimized initially. Growth temperature optimization was conducted by analyzing the carbon layer grown at temperatures ranging from 150 to 650 °C using XPS characterization. For this reason, the ratio of sp<sup>2</sup> carbon to sp carbon was used as a criterion to select the optimum growth temperature (Figure S3, Supporting Information).

To assess the structural and qualitative aspects of the HsGDY, we conducted meticulous microscopic and spectroscopic analyses of the HsGDY grown under optimized growth conditions. Figure S4a (Supporting Information) shows a camera image of 1 cm<sup>2</sup>-sized HsGDY transferred on 300 nm SiO<sub>2</sub>/Si. The optical microscopic image (Figure 1b), as well as the SEM image (Figure S4b, Supporting Information) of the HsGDY on a Si substrate with a 300 nm oxide layer, displayed a clean layer without physical defects (e.g., cracks or tearing).

In addition, the transmittance as obtained from UV-vis spectra in Figure 1c displayed a value of 91.2% at 500 nm, which is well-matched with the transmittance observed for other bilayer carbon layers.<sup>[35]</sup> The high optical transparency indicates the potential applicability of Bi-HsGDY in transparent electronics. Next, since uniformity is one of the important requirements for flexible electronics, AFM was performed to check the root mean square (RMS) roughness of the HsGDY, and it was found to be  $\approx 1.03 \text{ nm}$  over an area of  $25 \mu\text{m}^2$ . Also, the 3D AFM image showed no tears or cracks, confirming the uniformity of the HsGDY layer (Figure 1d). In addition, the thickness of the HsGDY was obtained as 1.4 nm, proving the bilayer nature of HsGDY layers (Figure 1e).<sup>[26,36]</sup>

The Raman spectra revealed the presence of characteristic bands related to the defects and graphitic linkages, at  $1349 \text{ cm}^{-1}$  (D band) and  $1599 \text{ cm}^{-1}$  (G band), respectively (Figure 1f). The  $I_D/I_G$  band intensity ratio of Bi-HsGDY was calculated to be 0.94, indicating a high degree of graphitization and few defect densities which displays the high quality of the Bi-HsGDY.<sup>[37,38]</sup> To check the uniformity of the Bi-HsGDY, Raman mapping was conducted according to the peak information obtained from the Raman spectra. Uniform mapping data were obtained, proving the uniformity of the Bi-HsGDY (Figure 1g). In addition, to ensure uniformity across all sample areas, Raman mapping (in  $25 \times 25 \mu\text{m}^2$  areas) was conducted throughout the sample. Corresponding results are depicted in Figure S5a–c (Supporting Information). Based on these findings, it is evident that the HsGDY layer exhibits consistent and high-quality growth across all regions, making it highly suitable for extensive large-area applications.

Following this, various spectroscopic studies were carried out to check the elementary composition and bonding structure of the Bi-HsGDY. To verify the chemical states of the as-grown Bi-HsGDY, XPS was employed as shown in Figure 2a,b. The XPS survey scan reveals core level peaks of O1s, C1s, and Ge3d centered at 531.8, 284.6, and 30.6 eV, respectively.<sup>[39]</sup> Deconvolution of the asymmetric C1s core peak unraveled the presence of three component peaks located at 284.7, 285.7, and 288.2 eV corresponding to carbon-carbon (C=C) double bonds, carbon-carbon (C≡C) triple bonds, and carbon-oxygen (C—O) single bonds, respectively.<sup>[40]</sup> The XPS data established the presence of both double and

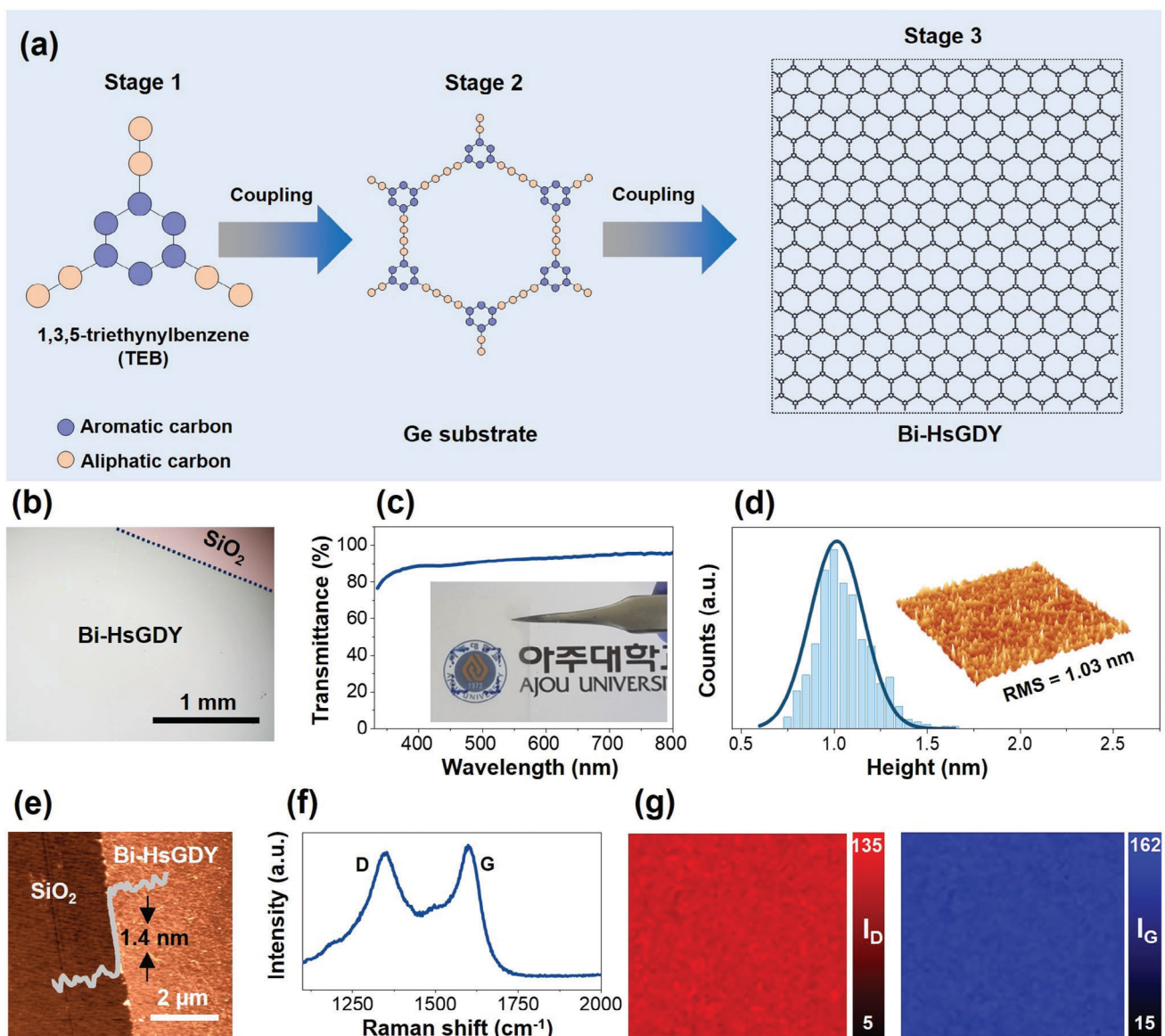


**Figure 1.** a) Schematic of the growth mechanism of Bi-HsGDY on Ge substrate. b) Optical image of Bi-HsGDY transferred onto a  $300\text{ nm } SiO_2$ /PET substrate. c) Transmittance of Bi-HsGDY in the range of  $300\text{--}800\text{ nm}$  (the inset shows the camera image of Bi-HsGDY/PET). d) Surface roughness of Bi-HsGDY scanned over  $25\text{ }\mu m^2$  (the inset shows the corresponding 3D AFM images) and e) 2D AFM image of Bi-HsGDY. f) Raman spectra and g) Raman mapping of the defect (D) and graphitic (G) bands of Bi-HsGDY.

triple-bonded carbons with ratios of their peak area as almost 1:1, which is in great agreement with the chemical structure of Bi-HsGDY (Figure 2b).<sup>[41]</sup> The presence of carbon-oxygen bonds indicated by XPS can be explained to be a consequence of the chemical adsorption of oxygen molecules onto the surface of the Bi-HsGDY due to exposure to atmospheric moisture.<sup>[42]</sup> Also, to confirm the complete etching of Ge by chemical agents and to rule out the presence of any Ge contamination in the Bi-HsGDY, Raman intensity maps were obtained for the Ge peak which is located at  $292\text{ cm}^{-1}$ . Raman mapping showed that the Ge etching process was perfectly accomplished and the Bi-HsGDY was free of contaminants (Figure S6, Supporting Information).<sup>[43]</sup>

The FT-IR spectra showed the band for the skeletal vibrations of aromatic moieties at  $1510\text{ cm}^{-1}$  and the characteristic band for the stretching vibration of the carbon-carbon ( $C\equiv C$ ) triple bonds at  $2180\text{ cm}^{-1}$  (Figure 2c), which confirmed the presence of diacetylenic linkages in the Bi-HsGDY. In addition, bands present at  $1010$ ,  $1160$ , and  $1380\text{ cm}^{-1}$  were related to the non-symmetric stretching of carbon-carbon ( $C-C$ ) single bonds, and aromatic hydrogen atoms caused the band at  $779\text{ cm}^{-1}$ .<sup>[40]</sup> Subsequently, the crystallinity of the Bi-HsGDY was analyzed using TEM, which confirmed its polycrystalline nature. In addition, a d-spacing of  $0.33\text{ nm}$  was observed, which corresponds to the (002) crystal plane of HsGDY as quoted in the literature (Figure 2d).<sup>[44,45]</sup>

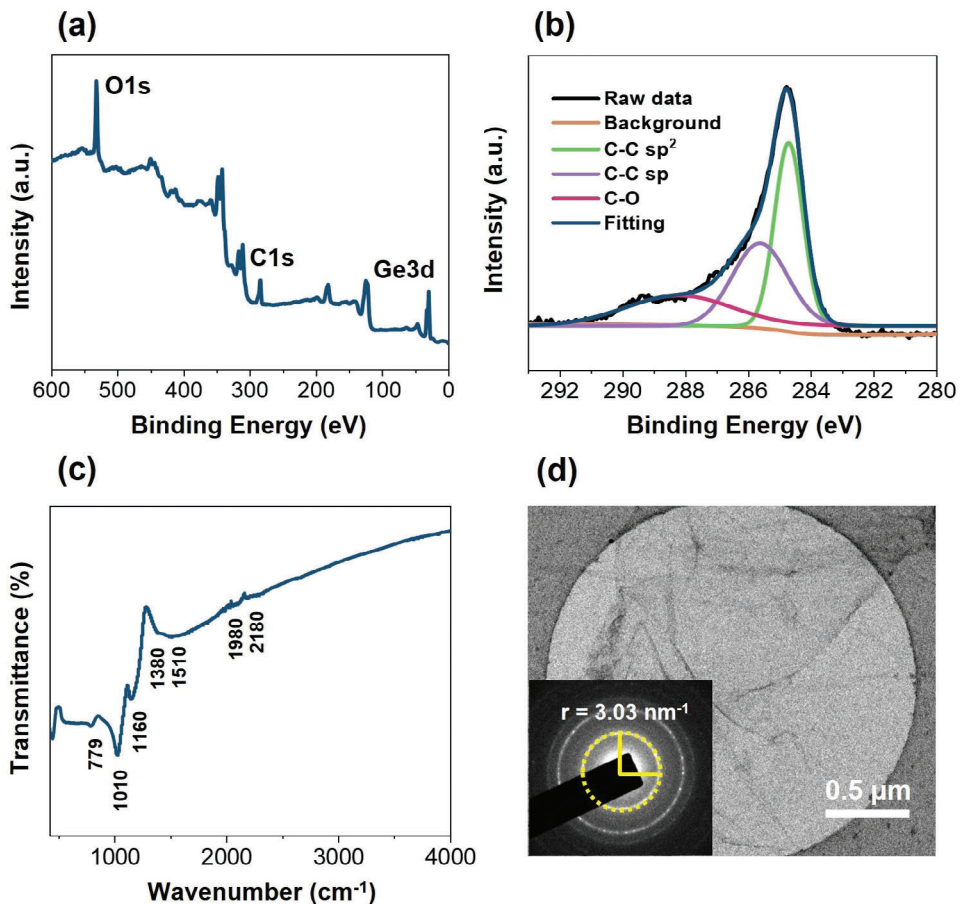


**Figure 2.** Characterizations of Bi-HsGDY. a) XPS spectra of Bi-HsGDY and b) Deconvoluted XPS spectra depicting the C1s band. c) FT-IR spectra of Bi-HsGDY. d) TEM image of Bi-HsGDY. The inset displays the SAED pattern confirming the poly-crystallinity of Bi-HsGDY.

As discussed previously, one of the notable characteristics of Bi-HsGDY grown on Ge substrate by the CVD method was the substantial size and high-quality bilayer of this material. To verify this assertion, Bi-HsGDY devices were constructed, and a series of electronic measurements were subsequently performed on them. These measurements aimed to thoroughly assess the performance and properties of the Bi-HsGDY, thereby shedding light on its potential applications. **Figure 3a** provides a schematic representation of the device on a SiO<sub>2</sub>/Si substrate and depicts the location of the source, drain, and gate electrodes.

Figure 3b shows an I-V plot obtained from the device. The source-drain current ( $I_{ds}$ ) between Au electrodes showed values of 60–80 μA, which is an ideal value considering the Bi-HsGDY and also the distance of ≈100 μm between electrodes. To further analyze the electrical resistance of Bi-HsGDY, the contact and sheet resistances were calculated from the transmission line method using the following Equation (1):

$$R_{\text{Total}} W = R_{\text{sheet}} L + 2R_C W \quad (1)$$

For this purpose, various contact distances were employed to assess both the contact resistance ( $R_C$ ) and sheet resistance ( $R_{\text{sheet}}$ ) of the device.<sup>[46]</sup> Figure 3c presents the total resistance ( $R_{\text{Total}}$ ) of the device as a function of contact lengths of the de-

vice. According to the relationship outlined in Equation (1), the width measured from the origin of the diagram in Figure 3c corresponds to  $2R_C$ . Therefore, based on these calculations, the value of the contact resistance can be determined as  $10 \Omega \mu\text{m}$ . This value of contact resistance is excellent for the interface between metal electrodes and carbon materials. For instance, in the 1D contact between graphene and Au, the contact resistance is  $2 \text{ k}\Omega \mu\text{m}$  (200 times higher than that of 2D contact for Bi-HsGDY).<sup>[47]</sup> The low contact resistance of Bi-HsGDY can be attributed to the close work function alignment between Bi-HsGDY and the metal (shown in Figure 4d), thereby enhancing the sensitivity of Bi-HsGDY-based devices compared to other devices.<sup>[48–51]</sup> Furthermore, the value of sheet resistance is  $3 \text{ k}\Omega \text{ sq}^{-1}$ , considering the large area of the device, seems reasonable, which ensures proper performance of devices fabricated based on Bi-HsGDY over a large lateral area. Also, Figure S7 (Supporting Information) illustrates the I-V plot obtained from the device with long distances (1, 0.7, and 0.5 mm) between metal contacts. Notably, a remarkable current of 10 μA was achieved at a bias voltage of +2 V with a contact distance of 0.5 mm, indicating the exceptional quality of the Bi-HsGDY and the ability of this material to be used in large-area electronic applications.

In addition, to check the electrostatic doping properties of Bi-HsGDY, and investigate the mobility of the structure, the gate

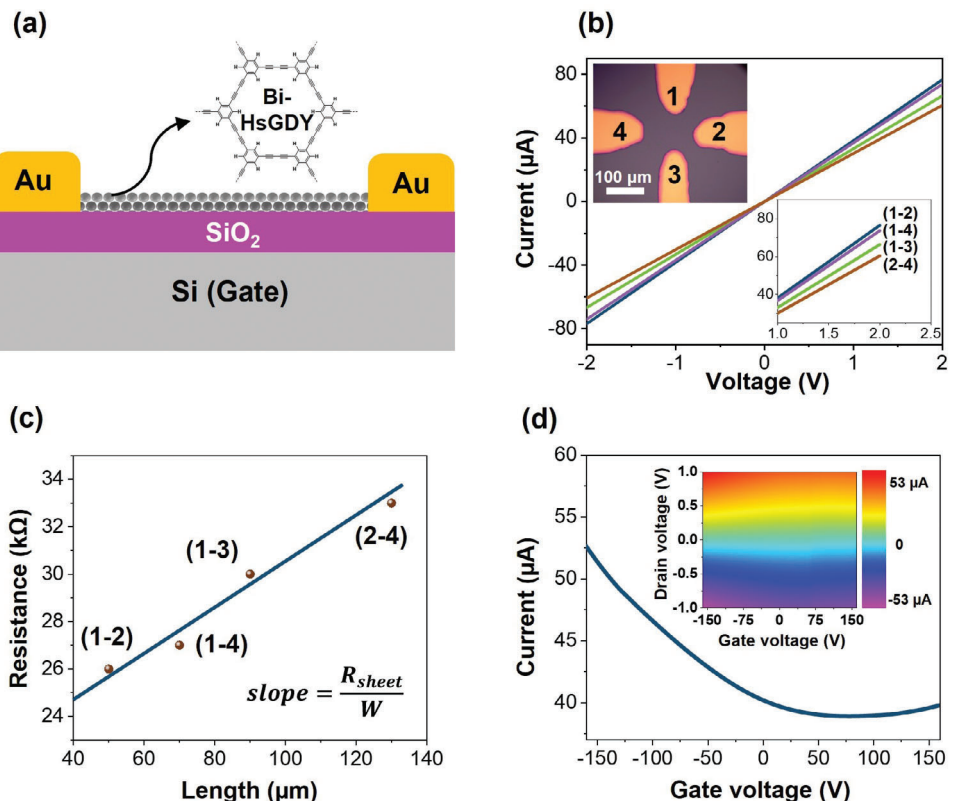


**Figure 3.** Investigations on the electrical properties of as-grown Bi-HsGDY. a) Schematic of the field effect transistor (FET) based on Bi-HsGDY. b) I–V plots for Bi-HsGDY with different contact distances (inset optical image). c) Contact and sheet resistance calculation of Bi-HsGDY device using different contact distances. d) Transport characteristics of the Bi-HsGDY FET and the inset display the effect of gate voltage ( $V_g$ ) in different biases.

voltage effect was measured. Figure 3d showcases the impact of gate voltage ( $V_g$ ) on the Bi-HsGDY structure. The observed low on/off ratio ( $\approx 1.3$ ) can be attributed to both the intrinsic characteristics of the synthesized HsGDY<sup>[26,52]</sup> and the design intricacies of the manufactured device (long-distance contacts). Also, Figure S8 (Supporting Information) displays the gate leakage current curve, demonstrating its negligible effect on the gate voltage results.

To determine the field-effect mobility, the linear region of the gate voltage curve can be utilized, employing the following Equation (2):

$$\mu = [dI_{ds}/dV_g] \times [L / (WC_i V_{ds})] \quad (2)$$

where  $L$  and  $W$  represent channel length and width, respectively.  $C_i$  is the capacitance of the insulating layer (300 nm SiO<sub>2</sub>), and  $C_{SiO_2}$  is  $\approx 1.15 \times 10^{-8} \text{ F cm}^{-2}$  for this device.<sup>[53]</sup> At  $V_{sd} = +1 \text{ V}$ , the efficient transport mobility of the Bi-HsGDY device was  $52.6 \text{ cm}^2 \text{ V}^{-1} \text{ s}^{-1}$ . Also, the inset of Figure 3d shows the effect of gate voltage in different biases from  $+1 \text{ V}$  to  $-1 \text{ V}$ . Furthermore, to check the stability of the constructed Bi-HsGDY devices in harsh conditions (high temperature), thermal stability measurements were conducted (Figure S9, Supporting Information). The results illustrate the stability results of the material up to 523 K.

In addition, to investigate the electrical properties of the synthesized HsGDY, Hall measurements have been conducted (Section S10, Supporting Information). The majority of charge

carriers are holes (p-type) with a carrier concentration of  $(2.11 \pm 0.19) \times 10^{14} \text{ cm}^{-2}$ . Also, the conductivity of the samples shows a high value of  $333.3 \pm 0.2 \text{ S cm}^{-1}$ , owing to the extensive conjugated network structure of HsGDY. The elevated conductivity in HsGDY is attributed to a very high carrier concentration, marking a notable twofold increase compared to previous experimental findings for HsGDY samples ( $\approx 5 \times 10^{12} \text{ cm}^{-2}$ ).<sup>[54]</sup>

The electrical properties of devices utilizing HsGDY reveal notable characteristics such as high conductivity and low  $R_C$ . To delve into a more comprehensive understanding of this phenomenon, an analysis of the band structure becomes imperative. Consequently, Density Functional Theory (DFT) calculations were employed to examine the structural and electronic properties of this material. The method section provides comprehensive details on the calculation procedures. Also, Figure 4a illustrates the unit cell implemented for this simulation. The simulation results consisting of the band structure and Density of States (DOS) are presented in Figure 4b. Notably, these results reveal a bandgap of 2.33 eV, aligning well with findings from other research papers.<sup>[16,55]</sup>

Also, we conducted an ultraviolet photoelectron microscopy (UPS) analysis to assess the work function (WF) of Bi-HsGDY. The UPS analysis results reveal a WF of 5.89 eV for Bi-HsGDY (Figure 4c). Utilizing this information, we can depict the band bending in the connection area of HsGDY with the Au contacts (Figure 4d). Based on the p-type nature of HsGDY and 0.59 eV bending at the interface connection, hole carriers emerge as the

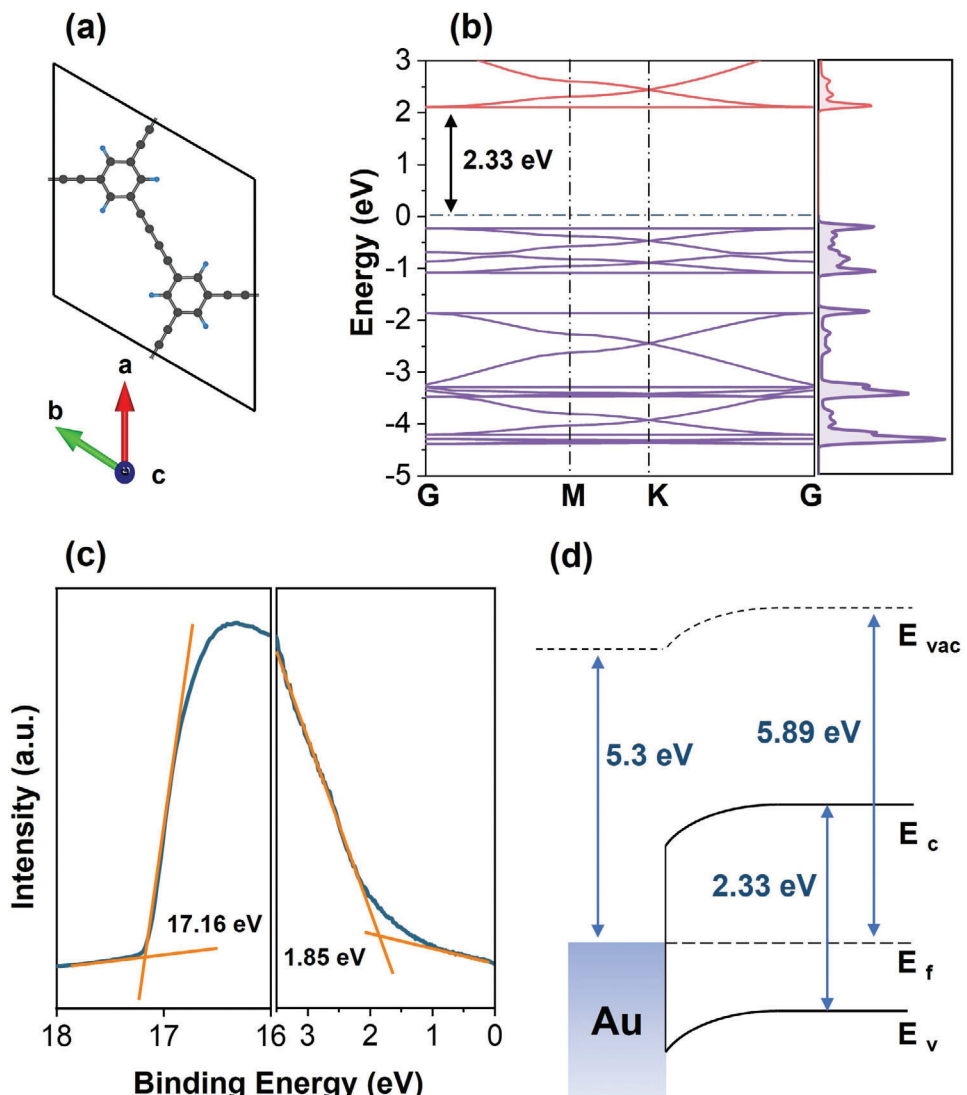


**Figure 4.** Band structure of Bi-HsGDY. a) The unit cell of the HsGDY structure. b) Band structure and DOS of charge carriers. c) UPS spectra of Bi-HsGDY. d) Band bending of Au/Bi-HsGDY.

dominant carriers in this structure, facilitating their efficient participation in conduction. This aspect contributes to the reduction of  $R_C$ , underscoring its significance in enhancing device performance. In addition, the presence of mid-gap states was discerned from the UPS spectra which could be a plausible explanation for the high hole concentration of Bi-HsGDY (Figure S10, Supporting Information).

The phenomenal electronic properties of large-area Bi-HsGDY hint at their huge potential in long-distance strain sensors. For exploring this purpose, Bi-HsGDY grown on Ge (110) wafers were transferred onto PET substrates to illustrate the electromechanical response of the Bi-HsGDY to bending strain in tensile and compressive directions. The large area of Bi-HsGDY makes it possible to place conductive contacts at long distances. This is a significant advantage of Bi-HsGDY for strain sensor applications as it can enhance the sensitivity of the GDY-based device to bending. The electrodes for this sensor were fabricated using

conductive silver paste. **Figure 5a** provides camera images of the Bi-HsGDY strain sensor (left) with normal (top right) and bent (bottom right) configurations.

Normalized resistance variations were calculated as  $\Delta R/R_0$ , where  $\Delta R$  is the difference in resistance ( $R-R_0$ ),  $R$  is the resistance after and  $R_0$  is the resistance before bending. When tensile bending was applied to the Bi-HsGDY/PET at a frequency of 1 Hz, normalized resistance variations ( $\Delta R/R_0$ ) progressively increased with an increment in bending angle. The  $\Delta R/R_0$  values were  $\approx 10$ , 15, and 18 for tensile strains of 0.36%, 0.40%, and 0.44%, respectively. On the other hand, when compressive bending was performed for PET-supported Bi-HsGDY, a step-wise decrease of  $\Delta R/R_0$  term was observed, showing the normalized resistance changes of -9, -15, and -18 for the compressive strains of -0.36%, -0.40%, and -0.44%, respectively. An almost symmetrical response was observed in both tensile and compressive directions, showing the sensitivity of the Bi-HsGDY strain

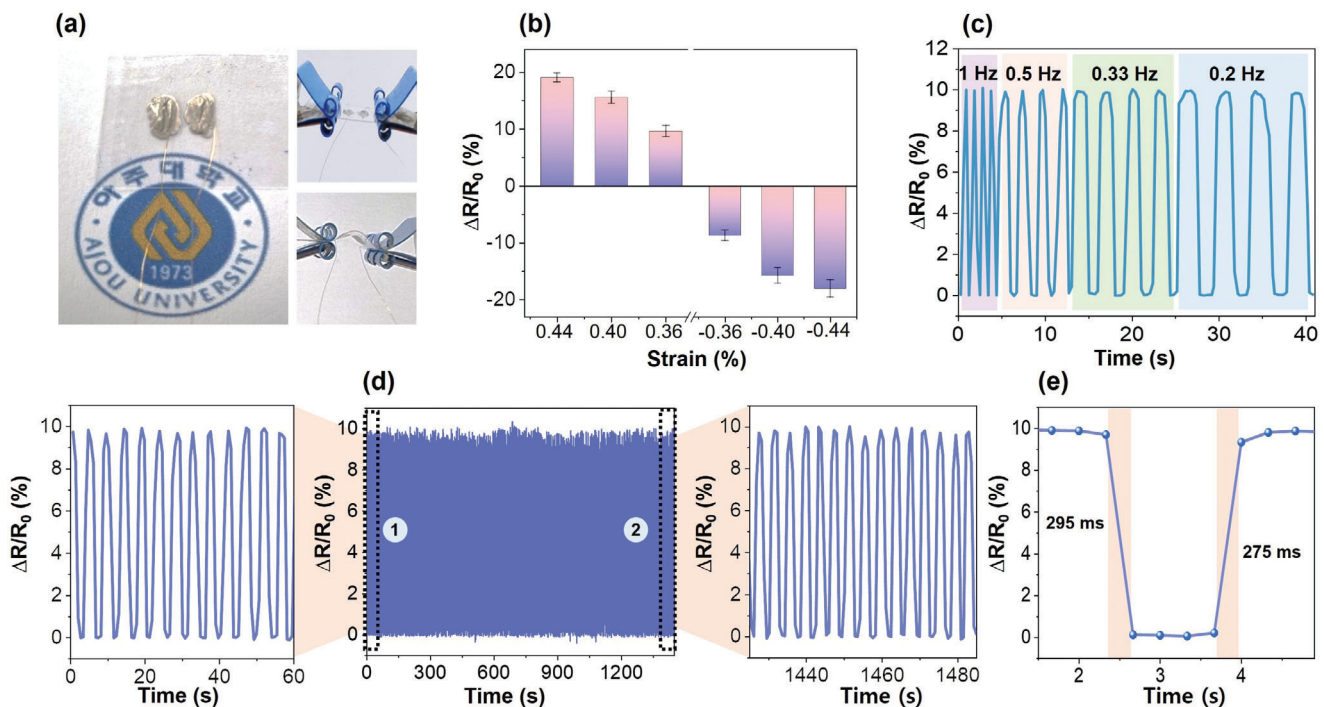


**Figure 5.** Effect of mechanical strain on Bi-HsGDY strain sensor. a) Camera images of the Bi-HsGDY strain sensor (left) in rest (top right) and bent (bottom right) positions. b) Plot of normalized resistance variation for various tensile and compressive strains. And c) Normalized resistance variation versus time for various frequencies. d) Durability check of Bi-HsGDY strain sensor for 1500 s (center) and normalized resistance changes for initial 30 s (left) and final 30 s (right). e) Response and recovery time for Bi-HsGDY strain sensor.

sensor to both tensile and compressive forces. Figure 5b shows variations in  $\Delta R/R_0$  when applying bending strain are replicable and reversible without causing any mechanical damage to the Bi-HsGDY strain sensor.

One of the important parameters for strain sensors is the gauge factor. A schematic for the calculation of strain and gauge factors of the Bi-HsGDY piezoresistive strain sensor is shown in Figure S11 (Supporting Information). The strain experienced by the Bi-HsGDY thin film during mechanical bending in both directions was calculated using the following Equation (3):

$$\varepsilon = \pm d_s / 2R \quad (3)$$

where  $d_s$  is the thickness of the substrate (100  $\mu\text{m}$ ) and  $R$  represents the radius of curvature of the device in a strained position.<sup>[20]</sup> Also, the gauge factor (GF) of the Bi-HsGDY strain sensor for the bending strains was calculated to assess the device's sensitivity using the following Equation (4):

$$\text{GF} = (\Delta R/R_0)/\varepsilon \quad (4)$$

In this relation,  $\Delta R/R_0$  is the normalized resistance change measured experimentally and  $\varepsilon$  is the strain experienced by the sensor as calculated using Equation (3).<sup>[56]</sup> The maximum GFs calculated for the Bi-HsGDY strain sensor were +43.34 and -43.14 under tensile and compressive strains, respectively. The variation in GF with an increased strain is shown in Figure S12 (Supporting Information).

As evident, HsGDY exhibits a notable strain responsivity, likely attributed to the presence of grain boundaries and low resistance within the structure of the HsGDY device: 1) the presence of grain boundaries in 2D materials typically introduces additional resistance, posing challenges to the efficient transport of charge carriers within the structure. However, during bending, the existence of these grain boundaries induces the hopping of charge carriers, which can improve the strain sensitivity of the structure. Hence, the existence of grain boundaries appears essential for increasing strain sensitivity.<sup>[20]</sup> 2) The sample's resistance significantly influences strain sensitivity. The presence of grain boundaries, cracks, and defects can hinder the transportation and mobility of charge carriers, thereby decreasing the electrical current level and consequently reducing the strain sensitivity of the structure.

Therefore, to enhance strain sensitivity, a dynamic interplay exists between the number of grain boundaries. In the synthesized Bi-HsGDY structure, the TEM results indicate its polycrystalline nature, which has an appropriate number of grain boundaries to generate the hopping of charge carriers. Also, the uniformity of the structure, coupled with the absence of cracks and defects in Bi-HsGDY, maintains the high gauge factor in the strain sensor.

Also, one important parameter for strain sensors is the elastic constant which is related to the flexibility of the material. To check this parameter, we performed COMSOL simulations, which revealed the high elastic constant of Bi-HsGDY (279 GPa) indicating the high capability of this material for strain sensors (Figure S13, Supporting Information).

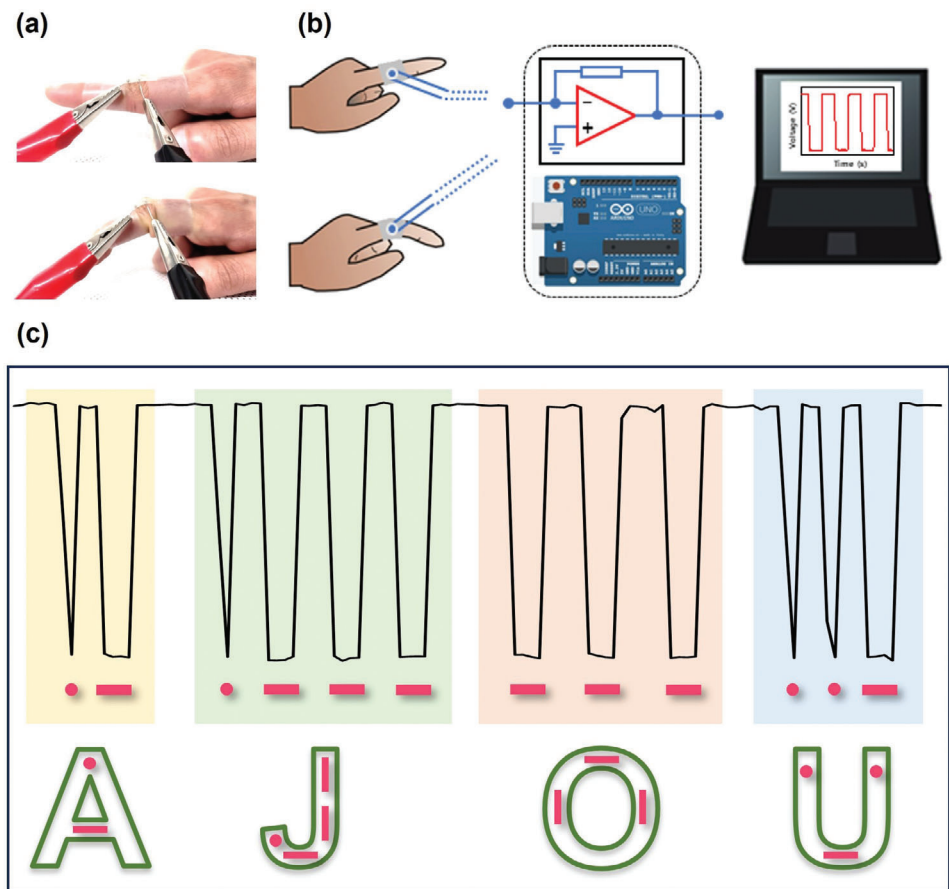


**Figure 6.** Morse code generation by Bi-HsG DY strain sensor. a) Camera images showing normal (top) and bent (bottom) configurations of a finger with the Bi-HsG DY strain sensor attached, generating “dash” and “dot” signals. b) Schematic for Morse code communication using Bi-HsG DY strain sensor. c) Morse signals generated by the Bi-HsG DY strain sensor spelling out the name “AJOU”.

Figure 5c illustrates  $\Delta R/R_0$  values for a strain of 0.36% in tensile direction for different bending frequencies (1, 0.5, 0.33, and 0.2 Hz). The  $\Delta R/R_0$  values were observed to be nearly constant irrespective of the bending frequency for the same applied tensile strain, indicating the appropriate responsivity of the device by applying bending strain. Figure 5d (center) shows the stability results for the Bi-HsG DY strain sensor by performing continuous bending for 1500 s at a tensile bending strain of 0.36% and a bending frequency of 0.2 Hz. An enlarged view of regions 1 and 2, which represent bending cycles during the first and last minutes, respectively, are provided in Figure 5d (left and right), confirming the dynamic and repeatable results for a long time frame. The rising and falling times for the sensor at a bending frequency of 0.2 Hz and a bending strain of 0.36% were measured as 275 and 295 ms, respectively. Response and recovery times were much less than one second, indicating a fast response to bending strain (Figure 5e). In addition, the strain sensor did not undergo any electrical failure during the bending processes, confirming the great adhesion of highly flexible Bi-HsG DY on the transparent PET substrate. Also, the effect of substrate thickness on the strain sensing performance of the device was evaluated by fabricating Bi-HsG DY/75  $\mu\text{m}$  PET strain sensors (Figure S14, Supporting Information).

To explore the practical application of Bi-HsG DY strain sensors in communication systems, a long-distance Bi-HsG DY strain sensor was used to generate Morse code. For more than a century, Morse code was an important means of communication, especially in military and maritime communications, providing fast and comprehensive transmission over long distances. Despite the prevalence of cutting-edge communication technologies, Morse code endures as a valuable fallback and specialized means of communication. It offers efficient and sturdy transmission, universal comprehension, and unwavering resilience during critical moments or when other communication systems falter. Within this intricately designed system, a correlation between the English alphabet and a sequence of “dashes” and “dots”, or their amalgamations has been established. In this study, we demonstrated the practical application of the long-distance Bi-HsG DY strain sensor in facilitating Morse code communication. Figure 6a, illustrates a finger in both its normal and bent positions, that effectively generates “dash” and “dot” signals. To decipher the Morse code, we conducted an investigation into the variations in current that occurred when the Bi-HsG DY strain sensor underwent discrete bending (indicating a “dot”) and continuous bending (indicating a “dash”). By exploring different combinations of these bending patterns, we successfully

**Table 1.** Comparison of strain sensor parameters of Bi-HsGDY/PET with similar reported devices.

Materials	Thickness	Crystallinity	Sensitivity (Gauge Factor)	Refs.
Heptazole film	Multilayer (55 nm)	Polycrystalline	1.51	[57]
Rubrene	Bulk (200 nm)	Single crystalline	279	[58]
Pentacene	Multilayer (70 nm)	Polycrystalline	12.5	[59]
MoO <sub>2</sub> nanosheets	Multilayer (86.1 nm)	Single crystalline	1.39	[60]
Gr-PEDOT:PSS /MnO <sub>2</sub> nanowires/Ecoflex composite	Bulk (1 mm)	–	0.8	[61]
Black P-Au	–	Single crystalline	1.5	[62]
Gallium selenide (GaSe)	Few layers	Single crystalline	4.3	[63]
HsGDY	Few layers (9.5 nm)	–	9.48	[20]
HsGDY	Multilayer (18 nm)	–	20.92	
Bi-HsGDY	Bilayer (1.4 nm)	Polycrystalline	43.34	This work

formulated the Morse code representation using the Bi-HsGDY strain sensor.

By introducing specific bends in the Bi-HsGDY strain sensor, we were able to generate distinct “dot” and “dash” signals, which were subsequently converted into electrical voltage signals using a current-to-voltage circuit. In this particular setup, the reading voltage was captured by an Arduino board and transmitted to a computer, enabling seamless communication as shown in Figure 6b. Furthermore, Figure S15 (Supporting Information) visually shows signals produced for the English vowels (A, E, I, O, and U), demonstrating the efficiency of the system, and Figure 6c demonstrates the Morse code signals generated to spell out the name of our university “AJOU”. These results provide compelling evidence for the high performance of long-distance Bi-HsGDY strain sensors in practical electronic applications. Moreover, these findings open up exciting possibilities for future applications of Bi-HsGDY in various domains that demand high levels of sensitivity to strain and show the role of long-distance contacts in the high sensitivity of the strain sensor.

**Table 1** lists the strain sensitivity of some organic strain sensors, 2D materials with similar structures as well as other HsGDY to the Bi-HsGDY sensor. It can be observed that the GF of the long-distance Bi-HsGDY sensor is 43.34, which is impressive and higher than the values reported for other 2D materials such as MoO<sub>2</sub>, MnO<sub>2</sub>, black P, and GaSe with similar band gaps. Therefore, from this comparison, Bi-HsGDY is understood to be a promising candidate for strain sensing with high sensitivity.

### 3. Conclusion

In summary, the controllable growth of Bi-HsGDY on Ge substrate by using TEB precursor through the low-temperature CVD method was realized successfully, which provides a highly efficient way for the synthesis of centimeter-sized, uniform Bi-HsGDY. The FET device prepared from these Bi-HsGDY structures exhibited a high carrier mobility of 52.6 cm<sup>2</sup> V<sup>-1</sup> s<sup>-1</sup> and a low contact resistance value of 10 Ω μm. Moreover, due to its transparency as well as the superior electrical properties, the large area Bi-HsGDY was used for developing piezoresistive strain sensors that displayed enhanced electromechanical response to bending strain, with a fast response time of ≈275 ms and a high gauge factor of 43.34. Also, as one of the applica-

tions of these devices, the long-distance Bi-HsGDY strain sensor was used to generate Morse code using the bending of the finger. The future of Bi-HsGDY in strain sensors and other flexible electronic applications can be improved by functionalizing the Bi-HsGDY or using it in conjunction with other 2D materials in a heterostructure format.

### 4. Experimental Section

**Synthesis of Bi-HsGDY:** Ge (110) wafers were used as growth substrates. These substrates were cleaned by ultrasonication in a series of solvents, sequentially (acetone, ethanol, and deionized water), dried with an N<sub>2</sub> gun, and finally treated with O<sub>2</sub> plasma. The superficial oxide layer was removed by immersing the Ge wafers in 2% hydrofluoric acid (HF) for 5 min, followed by rinsing with deionized water and drying with an N<sub>2</sub> gun. An oxide etching process is performed immediately before inserting growth substrates into the CVD quartz tube.

A home-built two-zone CVD was used for the Bi-HsGDY synthesis, wherein TEB (precursor, purchased from Thermo Fisher Scientific) was kept in an alumina boat in the first zone and growth substrates mounted on a holder were placed in the second zone. Once the base pressure was brought down to  $8 \times 10^{-3}$  Torr, the temperature of the CVD system was ramped to 900 °C under the flow of 100 sccm H<sub>2</sub> gas. After 20 min of H<sub>2</sub> flow at high temperature, room temperature conditions were achieved by fast cooling. This step ensures a hydrogen-terminated surface on the Ge wafers which effectively passivates the surface of the substrate. Subsequently, temperatures of both zones were set to 60 °C and the desired growth temperatures (150 °C), respectively, and Bi-HsGDY growth was achieved in 120 min.

**Wet Transfer of Bi-HsGDY:** For transferring Bi-HsGDY, a polymethyl methacrylate (PMMA)-assisted wet transfer process was used.<sup>[64]</sup> The PMMA A4 solution was spin-coated onto Bi-HsGDY/Ge at 2000 rpm and then baked on a hotplate at 80 °C for 8 min. The PMMA/ Bi-HsGDY/Ge structure was then floated (PMMA side up) in Ge etchant (HF:H<sub>2</sub>O<sub>2</sub>:DI water = 1:1:4) for a few hours. Once the Ge wafer was fully etched off, the PMMA-supported Bi-HsGDY was scooped out from the etchant using a clean SiO<sub>2</sub>/Si wafer. Following this, the PMMA/Bi-HsGDY was cleaned well with deionized water several times to remove any residual etchant or impurities. It was then transferred onto the substrate of interest (SiO<sub>2</sub>/Si, PET, or Quartz). At this stage, to remove trapped water droplets between the Bi-HsGDY and substrate, the samples were dried at an inclined angle, and finally, to improve the adhesion between the Bi-HsGDY and the substrate, samples were baked at 100 °C for 12 h.

**Device Fabrication:** Electrical devices were fabricated to study the electronic properties of Bi-HsGDY. The device fabrication process included mainly three steps: 1) attaching a physical mask with desired electrode

patterns onto Bi-HsGDY/substrate; 2) deposition of metal electrodes (Cr/Au, 5 nm/100 nm) using an e-beam evaporator, and 3) detaching the physical mask to reveal patterned electrodes. Because of the centimeter-scale and uniform growth of Bi-HsGDY, strain sensor fabrication was performed via a simple one-step process using conductive silver paste as metal contact, without the use of physical or photo masks.

**Characterizations:** MFP-3D Infinity atomic force microscope (Oxford Instruments) was used to perform the atomic force microscopy (AFM) measurements to analyze the thickness and uniformity of the samples. Raman measurements were conducted using an inVia confocal Raman microscope (Renishaw) with an excitation wavelength of 532 nm at room temperature condition. X-ray photoelectron spectroscopy (XPS) studies were carried out using a NEXA spectrometer (Thermo Fisher Scientific) with monochromatic Al K $\alpha$  radiation to investigate the chemical states of the samples. The transmittance of Bi-HsGDY was measured using Rigol Ultra 3660 UV-vis spectrophotometer. The Nicolet iS50 (Thermo Fisher Scientific) was used for obtaining the Fourier transform infrared (FT-IR) spectra and the transmission electron microscope (TEM) studies were performed using JEOL JEM-2100F with an operating voltage of 200 kV. Morphology studies were performed using a JEOL JSM-7900F scanning electron microscope (SEM) with an accelerating voltage of 10 kV. To measure the work function (WF) of Bi-HsGDY, UV Photoelectron Spectroscopy (UPS) was performed using Nexsa (ThermoFisher Scientific) with a He $^+$  excitation source ( $\hbar\nu = 21.2$  eV). WF was calculated as:  $WF = \hbar\nu - (E_{SECO} - E_{VB})$ , where  $E_{SECO}$  is the secondary electron cut-off energy and  $E_{VB}$  is the energy of the valence band region near the Fermi level. All the electrical characterizations of Bi-HsGDY were conducted using a KEITHLEY 4200-SCS instrument.

**Simulations—DFT Calculation:** All the DFT calculations have been performed with the Vienna ab-initio simulation package (VASP).<sup>[65]</sup> The projector-augmented wave (PAW) method was used to take electron-ion interactions into account.<sup>[66]</sup> Also, the generalized gradient approximation (GGA) within the Perdew–Burke–Ernzerhof (PBE) was used for the exchange-correlation potential,<sup>[67]</sup> and a cutoff energy of 520 eV was used. For the Brillouin zone integration, a  $10 \times 10 \times 1$  Gamma-centered k-point mesh was used to ensure converged electronic results within PBE. For structure optimization, Hellmann–Feynman forces were in the range of 0.01 eV Å $^{-1}$ . The convergence criteria for the electronic self-consistence loop were set to be  $10^{-6}$  eV.

**Simulations—COMSOL Simulation:** The elastic constant was determined through a finite element method (FEM) analysis using COMSOL Multiphysics. In this simulation, a fixed boundary was established, an applied force was introduced to the free boundary, and the resulting deformation, quantified as static displacement, was measured. The elastic constant can be calculated using the following relation:

$$EA(\nabla.U) + F_V = 0 \quad (5)$$

In this equation,  $E$  represents the elastic constant,  $A$  denotes the force application area,  $U$  represents displacement, and  $F_V$  represents the applied force inducing strain.

## Supporting Information

Supporting Information is available from the Wiley Online Library or from the author.

## Acknowledgements

M.J.J. and S.G. contributed equally to this work. This work was supported by grants (NRF-2021R1A2C2012649, 2021M3H1A104892211, and RS-2023-00221295) of the National Research Foundation (NRF) and by the H2KOREA funded by the Ministry of Education (2022Hydrogen fuel cell-002, Innovative Human Resources Development Project for Hydrogen Fuel Cells), Republic of Korea.

## Conflict of Interest

The authors declare no conflict of interest.

## Data Availability Statement

The data that support the findings of this study are available from the corresponding author upon reasonable request.

## Keywords

chemical vapor deposition, hydrogen substituted graphdiyne, morse code, strain sensors, uniform growth

Received: August 22, 2023

Revised: December 21, 2023

Published online: January 9, 2024

- [1] W. Gao, H. Ota, D. Kiriya, K. Takei, A. Javey, *Acc. Chem. Res.* **2019**, *52*, 523.
- [2] V. Adepu, M. Tathacharya, R. Cs, V. Mattela, P. Sahatiya, *ACS Appl. Nano. Mater.* **2022**, *5*, 18209.
- [3] Q. Pang, D. Lou, S. Li, G. Wang, B. Qiao, S. Dong, L. Ma, C. Gao, Z. Wu, *Adv. Sci.* **2020**, *7*, 1902673.
- [4] D. T. Bird, N. M. Ravindra, *Polymers* **2021**, *13*, 1455.
- [5] G.-H. Zhang, L. Zhang, Q.-H. Zhu, H. Chen, W.-L. Yuan, J. Fu, S.-L. Wang, L. He, G.-H. Tao, *ACS Mater. Lett.* **2022**, *4*, 136.
- [6] X. Zhang, Y. Zhang, H. Yu, H. Zhao, Z. Cao, Z. Zhang, Y. Zhang, *Adv. Mater.* **2023**, *35*, 2207966.
- [7] S. Venkateshwaran, M. J. Josline, S. M. Senthil Kumar, *Int. J. Hydrog. Energy* **2021**, *46*, 8377.
- [8] S. Ghods, A. Esfandiar, A. Iraji Zad, S. Vardast, *ACS Omega* **2022**, *7*, 2091.
- [9] L. Gao, *Small* **2017**, *13*, 1603994.
- [10] S. Ghods, A. Esfandiar, J.-H. Choi, A. Iraji Zad, M. J. Josline, S. Kim, J.-H. Lee, *Mater. Today Phys.* **2023**, *30*, 101235.
- [11] A. Hirsch, *Nat. Mater.* **2010**, *9*, 868.
- [12] F. Liu, W. T. Navaraj, N. Yogeswaran, D. H. Gregory, R. Dahiya, *ACS Nano* **2019**, *13*, 3257.
- [13] W. Zhang, C. Chai, Q. Fan, Y. Song, Y. Yang, *Appl. Surf. Sci.* **2021**, *537*, 147885.
- [14] H. W. Choi, K.-B. Nam, D.-W. Shin, *Adv. Mater. Interfaces* **2023**, *10*, 2202489.
- [15] M. J. Josline, E.-T. Kim, J.-H. Lee, *Appl. Sci. Converg. Technol.* **2022**, *31*, 63.
- [16] J. Li, A. Slassi, X. Han, D. Cornil, M.-H. Ha-Thi, T. Pino, D. P. Debecker, C. Colbeau-Justin, J. Arbiol, J. Cornil, M. N. Ghazzal, *Adv. Funct. Mater.* **2021**, *31*, 2100994.
- [17] Z. Man, P. Li, S. Liu, Y. Zhang, X. Zhu, S. Ye, W. Lu, W. Chen, G. Wu, N. Bao, *ACS Appl. Mater. Interfaces* **2023**, *15*, 26910.
- [18] Q. Yang, Y. Guo, B. Yan, C. Wang, Z. Liu, Z. Huang, Y. Wang, Y. Li, H. Li, L. Song, J. Fan, C. Zhi, *Adv. Mater.* **2020**, *32*, 2001755.
- [19] X. Ren, X. Li, Z. Yang, X. Wang, J. He, K. Wang, J. Yin, J. Li, C. Huang, *ACS Sustainable Chem. Eng.* **2020**, *8*, 2614.
- [20] Y. Cai, J. Shen, J.-H. Fu, N. Qaiser, C. Chen, C.-C. Tseng, M. Hakami, Z. Yang, H.-J. Yen, X. Dong, L.-J. Li, Y. Han, V. Tung, *ACS Nano* **2022**, *16*, 16677.
- [21] S. Zhang, J. Wang, Z. Li, R. Zhao, L. Tong, Z. Liu, J. Zhang, Z. Liu, *J. Phys. Chem. C* **2016**, *120*, 10605.
- [22] M. Desroches, M.-A. Courtemanche, G. Rioux, J.-F. Morin, *J. Org. Chem.* **2015**, *80*, 10634.

- [23] X. Zhou, B. Fu, L. Li, Z. Tian, X. Xu, Z. Wu, J. Yang, Z. Zhang, *Nat. Commun.* **2022**, *13*, 5770.
- [24] W. Zhou, H. Shen, Y. Zeng, Y. Yi, Z. Zuo, Y. Li, Y. Li, *Angew. Chem., Int. Ed.* **2020**, *59*, 4908.
- [25] Y. Kong, J. Li, S. Zeng, C. Yin, L. Tong, J. Zhang, *Chem* **2020**, *6*, 1933.
- [26] R. Liu, X. Gao, J. Zhou, H. Xu, Z. Li, S. Zhang, Z. Xie, J. Zhang, Z. Liu, *Adv. Mater.* **2017**, *29*, 1604665.
- [27] J. Shen, Y. Cai, C. Zhang, W. Wei, C. Chen, L. Liu, K. Yang, Y. Ma, Y. Wang, C.-C. Tseng, J.-H. Fu, X. Dong, J. Li, X.-X. Zhang, L.-J. Li, J. Jiang, I. Pinnau, V. Tung, Y. Han, *Nat. Mater.* **2022**, *21*, 1183.
- [28] D. P. Do, C. Hong, V. Q. Bui, T. H. Pham, S. Seo, V. D. Do, T. L. Phan, K. M. Tran, S. Haldar, B.-W. Ahn, S. C. Lim, W. J. Yu, S.-G. Kim, J.-H. Kim, H. Lee, *Adv. Sci.* **2023**, *10*, 2300925.
- [29] J.-H. Lee, E. K. Lee, W.-J. Joo, Y. Jang, B.-S. Kim, J. Y. Lim, S.-H. Choi, S. J. Ahn, J. R. Ahn, M.-H. Park, C.-W. Yang, B. L. Choi, S.-W. Hwang, D. Whang, *Science* **2014**, *344*, 286.
- [30] M.-K. Hong, S.-H. Hyun, H.-S. Jang, B.-S. An, H.-C. Jang, H.-S. Hwang, S.-I. Kim, J.-Y. Moon, S. M. Sattari-Esfahlan, S.-Y. Lee, S.-K. Son, D. Whang, J.-H. Lee, *Appl. Surf. Sci.* **2021**, *554*, 149655.
- [31] T. Wang, P. Li, X. Hu, M. Gao, Z. Di, Z. Xue, M. Zhang, *Appl. Surf. Sci.* **2020**, *529*, 147066.
- [32] Y. Zhao, D. Han, X. Wang, Z. Hu, Y. Chen, Y. Chen, D. Zhou, Y. Li, E. G. Fu, Z. Zhao, *Carbon* **2019**, *153*, 776.
- [33] Y. T. Nam, H. Kang, S. Chong, Y.-J. Kim, W. Lee, Y. Lee, J. Kim, S.-Y. Cho, H.-T. Jung, *ACS Sens.* **2023**, *8*, 1151.
- [34] Y. Guo, J. Liu, Q. Yang, L. Ma, Y. Zhao, Z. Huang, X. Li, B. Dong, X.-Z. Fu, C. Zhi, *Small* **2020**, *16*, 1907341.
- [35] Q. Chen, Y. Zhong, M. Huang, G. Zhao, Z. Zhen, H. Zhu, *2D Mater.* **2018**, *5*, 035001.
- [36] J. Li, Y. Xiong, Z. Xie, X. Gao, J. Zhou, C. Yin, L. Tong, C. Chen, Z. Liu, J. Zhang, *ACS Appl. Mater. Interfaces* **2019**, *11*, 2734.
- [37] Y. Xue, J. Li, Z. Xue, Y. Li, H. Liu, D. Li, W. Yang, Y. Li, *ACS Appl. Mater. Interfaces* **2016**, *8*, 31083.
- [38] Y. Yue, Y. Xu, F. Kong, Q. Li, S. Ren, *Carbon* **2020**, *167*, 202.
- [39] D. Zhou, Z. Niu, T. Niu, *J. Phys. Chem. C* **2018**, *122*, 21874.
- [40] J. He, N. Wang, Z. Cui, H. Du, L. Fu, C. Huang, Z. Yang, X. Shen, Y. Yi, Z. Tu, Y. Li, *Nat. Commun.* **2017**, *8*, 1172.
- [41] Q. Lv, W. Si, J. He, L. Sun, C. Zhang, N. Wang, Z. Yang, X. Li, X. Wang, W. Deng, Y. Long, C. Huang, Y. Li, *Nat. Commun.* **2018**, *9*, 3376.
- [42] X. Yang, Z. Qu, S. Li, M. Peng, C. Li, R. Hua, H. Fan, J. Caro, H. Meng, *Angew. Chem., Int. Ed.* **2023**, *62*, e202217378.
- [43] M. Inoue, *Jpn. J. Appl. Phys.* **1972**, *11*, 1147.
- [44] C. Li, X. Lu, Y. Han, S. Tang, Y. Ding, R. Liu, H. Bao, Y. Li, J. Luo, T. Lu, *Nano Res.* **2018**, *11*, 1714.
- [45] W. Ding, M. Sun, Z. Zhang, X. Lin, B. Gao, *Ultrason. Sonochem.* **2020**, *61*, 104850.
- [46] P.-C. Shen, C. Su, Y. Lin, A.-S. Chou, C.-C. Cheng, J.-H. Park, M.-H. Chiu, A.-Y. Lu, H.-L. Tang, M. M. Tavakoli, G. Pitner, X. Ji, Z. Cai, N. Mao, J. Wang, V. Tung, J. Li, J. Bokor, A. Zettl, C.-I. Wu, T. Palacios, L.-J. Li, J. Kong, *Nature* **2021**, *593*, 211.
- [47] L. Wang, I. Meric, P. Y. Huang, Q. Gao, Y. Gao, H. Tran, T. Taniguchi, K. Watanabe, L. M. Campos, D. A. Muller, J. Guo, P. Kim, J. Hone, K. L. Shepard, C. R. Dean, *Science* **2013**, *342*, 614.
- [48] B. Hua, H. Kang, J. Zhong, X. Zhan, L. Xu, J. Li, Y. Zheng, Z. Zheng, *ACS Appl. Mater. Interfaces* **2021**, *13*, 34332.
- [49] M. Dehkhodaei, A. Reisi-Vanani, *Int. J. Hydrol. Energy* **2022**, *47*, 36886.
- [50] Y.-J. Yu, Y. Zhao, S. Ryu, L. E. Brus, K. S. Kim, P. Kim, *Nano Lett.* **2009**, *9*, 3430.
- [51] W. M. H. Sachtler, G. J. H. Dorgelo, A. A. Holscher, *Surf. Sci.* **1966**, *5*, 221.
- [52] J. Zhou, Z. Xie, R. Liu, X. Gao, J. Li, Y. Xiong, L. Tong, J. Zhang, Z. Liu, *ACS Appl. Mater. Interfaces* **2018**, *11*, 2632.
- [53] S. Ghods, S. Vardast, A. Esfandiar, A. Iraji Zad, M. Heidariramsheh, *ACS Appl. Electron. Mater.* **2022**, *4*, 6204.
- [54] Y. Li, M. Zhang, X. Hu, X. Fan, L. Yu, C. Huang, *J. Phys. Chem. Lett.* **2020**, *11*, 1998.
- [55] S. Debnath, C. Phan, D. J. Searles, M. Hankel, M. Hankel, *ACS Appl. Energy Mater.* **2020**, *3*, 7404.
- [56] P. Xue, C. Chen, D. Diao, *Carbon* **2019**, *147*, 227.
- [57] Y. Cho, P. J. Jeon, J. S. Kim, S. Im, *Org. Electron.* **2017**, *40*, 24.
- [58] H. Wang, Y. Tong, X. Zhao, Q. Tang, Y. Liu, *Org. Electron.* **2018**, *61*, 304.
- [59] D.-I. Kim, B.-U. Hwang, N. T. Tien, I.-J. Kim, N.-E. Lee, *Electron. Mater. Lett.* **2012**, *8*, 11.
- [60] H. Wu, P. Tong, B. Li, M. Tang, N. Wei, J. Zhao, *ACS Appl. Nano Mater.* **2023**, *6*, 16145.
- [61] M. Asad Ullah Khalid, S. Hwan Chang, *Compos. Struct.* **2023**, *311*, 116824.
- [62] H. Jiang, J. Zhang, M. Qin, J. Zhang, X. Zou, X. Weng, *Sens. Actuator A Phys.* **2023**, *356*, 114359.
- [63] C. Wang, S. X. Yang, H. R. Zhang, L. N. Du, L. Wang, F. Y. Yang, X. Z. Zhang, Q. Liu, *Front. Phys.* **2016**, *11*, 1.
- [64] S. Kim, S. Shin, T. Kim, H. Du, M. Song, C. Lee, K. Kim, S. Cho, D. H. Seo, S. Seo, *Carbon* **2016**, *98*, 352.
- [65] G. Kresse, J. Furthmüller, *Phys. Rev. B* **1996**, *54*, 11169.
- [66] P. E. Blöchl, *Phys. Rev. B* **1994**, *50*, 17953.
- [67] J. P. Perdew, K. Burke, M. Ernzerhof, *Phys. Rev. Lett.* **1996**, *77*, 3865.